Journal of Advanced Electrochemical Storage

ISSN (Online): 3139-7190

Indexed in www.pubj.org



Structural characterization and Charge density approximations of $LaAlO_3$ & $La_2Zr_2O_7$

G. Venkatesh[1,*]

[1]*Department of Metallurgical Engineering, PSG College of Technology, Coimbatore-641 004 Tamil Nadu, India.*

*Corresponding author: venkih07@gmail.com

DOI: https://doi.org/10.67977/jaes.vol.2.issue1.2

J. Adv. Electro. Storage 2(1) 2026 127–143



Keywords: $LaAlO_3$; $La_2Zr_2O_7$; Solid-state reaction; Rietveld refinement; Crystallographic modelling; Electron-density mapping; VESTA; Transmission electron microscopy.

Received 19th February 2026
Published 20th April 2026

Licensed under CC-BY 4.0



ABSTRACT: Lanthanum aluminate ($LaAlO_3$) and lanthanum zirconate ($La_2Zr_2O_7$) composite powders were synthesized by a conventional solid-state reaction using La_2O_3, Al_2O_3 and ZrO_2 as the starting materials, followed by wet ball milling and sintering at 1300 °C. Powder X-ray diffraction and Rietveld refinement were used for phase identification, quantitative phase analysis and determination of the crystallographic parameters. The refinement confirmed rhombohedral perovskite $LaAlO_3$ with the R3c space group as the major phase, accounting for approximately 95 wt%, whereas cubic pyrochlore $La_2Zr_2O_7$ with the Fd3m space group was identified as the minor phase, accounting for approximately 5 wt%. The refined structural parameters and structure factors were used for crystallographic modelling and electron-density analysis using FullProf and Visualization for Electronic and Structural Analysis (VESTA). The three-dimensional crystal structures, atomic coordination environments, bond lengths and electron-density distributions of both phases were examined. Fourier-based electron-density maps across selected crystallographic planes showed distinct charge-localization features around the La–O, Al–O and Zr–O coordination environments, indicating differences in the local bonding characteristics of the two crystalline phases. Transmission electron microscopy, high-resolution transmission electron microscopy and selected-area electron diffraction further confirmed the crystalline nature, phase formation and preferred crystallographic orientation of the synthesized powders. The combined Rietveld refinement, crystallographic modelling and electron-microscopy analyses provide a detailed description of the structural and electron-density characteristics of the $LaAlO_3$–$La_2Zr_2O_7$ composite system.

1. INTRODUCTION

Composite oxide systems containing lanthanum aluminate ($LaAlO_3$) and lanthanum zirconate ($La_2Zr_2O_7$) are structurally important because they combine two different crystallographic frameworks within the same ceramic powder. $LaAlO_3$ belongs to the ABO_3 perovskite family and generally crystallizes at room temperature in a rhombohedrally distorted structure with the R3c space group. In this structure, La^{3+} occupies the larger A site, while Al^{3+} occupies the B site within corner-connected AlO_6 octahedra. The rotation of these octahedra produces a small deviation from the

How to cite this article: G. Venkatesh. (2026). Structural characterization and Charge density approximations of $LaAlO_3$ & $La_2Zr_2O_7$, Journal of Advanced Electrochemical Storage, 2(1), 127–143. https://doi.org/10.67977/vol.2.issue1.2

ideal cubic perovskite structure and affects the Al–O bond distances, Al–O–Al bond angles and local La–O coordination. The formation and microstructure of $LaAlO_3$ are strongly influenced by the synthesis route and thermal treatment. Mechanochemical milling of La_2O_3 with transition alumina produced single-phase $LaAlO_3$ after 120 min of planetary milling, whereas the same reaction did not occur with less-reactive α-Al_2O_3 [1]. Molten-salt processing formed rhombohedral $LaAlO_3$ from equimolar La_2O_3 and Al_2O_3 at 630–800 °C within 3 h; the particle size increased from below 3 μm to approximately 3–7 μm when the temperature increased from 630 to 700 °C [2]. A polymerized-complex route produced phase-pure $LaAlO_3$ at 700 °C for 8 h or 750 °C for 2 h, with a specific surface area of 13–16 $m^2 g^{-1}$ compared with approximately 0.3 $m^2 g^{-1}$ for conventionally prepared powder [3]. Combustion synthesis also produced pure perovskite $LaAlO_3$ at 700 °C for 2 h with particle sizes of approximately 78–100 nm [4]. Convergent-beam electron diffraction has confirmed the rhombohedral R3c symmetry of $LaAlO_3$ and demonstrated the importance of electron-diffraction analysis in distinguishing it from a pseudocubic structural description [5]. More recent studies using XRD and Rietveld refinement obtained single-phase $LaAlO_3$ at temperatures ranging from 600 to 800 °C, depending on the precursor chemistry and synthesis route [6]. Coprecipitation produced phase-pure $LaAlO_3$ at approximately 835 °C, and the powder calcined at 900 °C for 2 h contained nearly isometric particles smaller than 15 nm [7]. Microwave-assisted combustion followed by short heat treatments at 700 and 900 °C has further shown that precursor chemistry and rapid thermal processing influence the crystallite size, unit-cell volume and local coordination geometry of the perovskite phase [8]. These studies collectively establish that $LaAlO_3$ possesses good chemical and high-temperature structural stability, but its phase purity, crystallite size and local structure remain sensitive to processing conditions [9].

$La_2Zr_2O_7$ belongs to the $A_2B_2O_7$ oxide family and commonly crystallizes as an ordered cubic pyrochlore with the Fd3m space group. Unlike the rhombohedral perovskite arrangement of $LaAlO_3$, the pyrochlore structure contains ordered La and Zr cation sublattices, Zr–O polyhedra and an ordered oxygen-vacancy arrangement. $La_2Zr_2O_7$ has been investigated as a high-temperature ceramic because it retains structural stability, exhibits low sintering activity and has lower thermal conductivity than conventional yttria-stabilized zirconia [10]. Long-term annealing at 1400 °C and repeated thermal cycling were reported to preserve the pyrochlore structure, although preferential grain growth and compositional changes may occur during plasma processing [11]. The degree of structural order in $A_2B_2O_7$ oxides is controlled by cation size and the energies associated with cation antisite and anion Frenkel disorder [12]. Planetary milling of La_2O_3 and ZrO_2 at 200 rpm for 12 h, followed by heat treatment at 1500 °C for 1 h, produced single-phase pyrochlore $La_2Zr_2O_7$, as confirmed by XRD and TEM [13]. Molten-salt synthesis reduced the formation temperature: phase-pure sub micrometre $La_2Zr_2O_7$ was obtained after 3 h at 1100 °C using a salt-to-reactant ratio of 5:1, or at 1200 °C using a ratio of 3:1 [14]. In coprecipitation processing, simultaneous precipitation of La and Zr from a basic solution produced a more homogeneous precursor and a highly crystalline $La_2Zr_2O_7$ phase; its measured thermal conductivity was approximately 50% lower than that of powder prepared through the less-homogeneous precipitation sequence [15]. Sol–gel combustion methods have produced pyrochlore $La_2Zr_2O_7$ nanocrystals with grain sizes of approximately 45–70 nm [16]. Direct comparison between defect-fluorite and pyrochlore $La_2Zr_2O_7$ has shown that the two phases possess the same chemical composition but differ in cation–anion ordering, oxygen-defect concentration and local Zr–O bonding environment [17]. Conventional solid-state sintering has also been shown to produce a stable pyrochlore phase in dense $La_2Zr_2O_7$ ceramics [18]. More recently, tartaric-acid-assisted coprecipitation produced defect-fluorite $La_2Zr_2O_7$ particles with an average size of 32.6 nm at 600 °C; increasing the calcination temperature to 800 °C transformed the material into pyrochlore $La_2Zr_2O_7$ with an average particle size of 68.4 nm [19]. Structural calculations have likewise indicated that changes in pressure, bond length and atomic ordering can move the pyrochlore arrangement towards a fluorite-like configuration [20]. The Rietveld refinement of the scale factors, background, lattice parameters, peak-profile parameters and structural variables, thereby allowing quantitative determination of the $LaAlO_3$ and $La_2Zr_2O_7$ phase fractions even when some diffraction peaks overlap [21]. FullProf provides full-pattern refinement and extraction of the calculated structure factors required for subsequent crystallographic analysis [22]. VESTA can use the refined lattice parameters, fractional atomic coordinates and structure factors to construct three-dimensional unit-cell models, display coordination polyhedra, calculate bond lengths and bond angles, generate Fourier and Patterson functions, and visualize electron-density distributions as two-dimensional sections or three-dimensional isosurfaces [23]. Pattern

decomposition and crystallographic information generated using EXPO further support the separation and modelling of individual phases within a multiphase powder [24]. The combined application of Rietveld refinement, VESTA-based electron-density mapping and TEM has previously been used to correlate average crystal structure with local crystallinity, lattice periodicity and elemental distribution [25].

The present work investigates $LaAlO_3$–$La_2Zr_2O_7$ composite powders synthesized by conventional solid-state reaction followed by mechanical milling and high-temperature sintering. XRD and Rietveld refinement are employed to identify and quantify the $LaAlO_3$ and $La_2Zr_2O_7$ phases and to obtain their refined crystallographic parameters. The refined structural models are subsequently used for three-dimensional crystallographic visualization and Fourier-based electron-density analysis using VESTA. TEM and HRTEM are used to evaluate the particle morphology and lattice periodicity, while SAED is used to confirm the indexed crystallographic planes and local orientation. EDS analysis is used to verify the presence of La, Al, Zr and O in the synthesized composite. Thus, the work provides an integrated crystallographic and microstructural comparison of two coexisting oxide phases with different structural symmetries and coordination environments.

2. Experimental procedure

$LaAl0_3$ and $La_2Zr_20_7$ were synthesized by the conventional solid-state reaction method from Al_20_3, La_20_3 and $Zr0_2$ mixture is taken in the ratio of 2:2:1 as shown in Figure 1. The raw materials used for this synthesis were all of 99.9% purity. The mixture was ground and crushed for 5 hours duration at wet condition (toluene), with the help of tungsten carbide balls in a planetary ball milling machine. After this process, the mixture was dried, compacted and sintered at the temperature of 1300°C to stabilize the $LaAl0_3$and $La_2Zr_20_7$ phases formed in the synthesized compound.

The sintered compound was characterized by X-ray powder diffraction analysis using Cu-Kα (1.54Å) radiation and are phase studied using High-Resolution Transmission electron microscopy (HR-TEM). The full pattern refinements for the obtained XRD data were carried out by means of the Rietveld method using the Panalytical X'pert High Score Plus [21]. Powder XRD had been chosen for analyzing the crystalline structures and quantifying the crystalline phases. The pseudo-Voigt function was used to model the profile, and a polynomial function was used to refine the background. From the Rietveld refinement, it was observed that no other phase had been present in the mixture, other than the $LaAl0_3$and $La_2Zr_20_7$. No fused zones between $LaAl0_3$ and $La_2Zr_20_7$was found in the XRD refinement. So, the refined results were then used for finding the electron density charge distribution across the planes involving both phases using GFourier program in FullProf software [22].

After this, the XRD pattern was subjected to pattern decomposition by the EXPO [23] and Panalytical X'pert High Score Plus software, in order to obtain the phases separately for further analysis. This process obtains the crystallographic information file for each phase. With this obtained information, the visualization of the 3D crystal structure for both phases was computed followed by charge density calculation. The charge density distribution across the symmetry planes was calculated by the Fourier synthesis of structure factors using VESTA [24]. Band structure and DOS for $LaAl0_3$were computed using the BURAI 1.3 software run by Quantum espresso database. The self-consistent field (SCF) method was adopted in this method with the ultrasoftpseudopotential. Brillouin zone values for the cubic lattice were considered for the calculation of the Band structure of $LaAl0_3$. SCF method calculation of

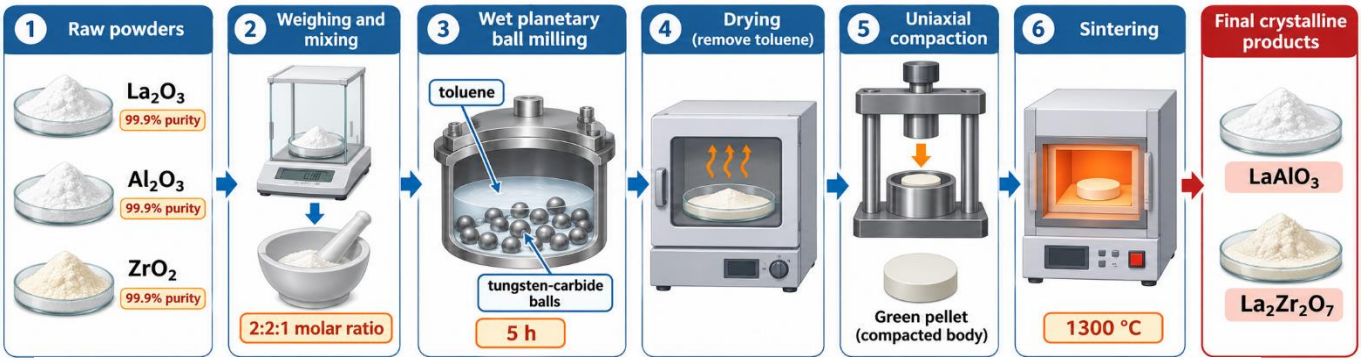


Figure 1 Preparation of $LaAl0_3$ and $La_2Zr_20_7$ by conventional solid-state reaction method.

$La_2Zr_2O_7$the phase was difficult to be computed, due to complexity (fusion of atoms) in the crystal structure. Therefore, the band structure and DOS of the $LaAlO_3$phase had been only reported with the charge density calculations of both phases.

3. RESULTS AND DISCUSSION

3.1. X-ray diffraction

Diffraction data were collected at room temperature on a SHIMADZU SPECTROMETER MODEL XRD 6000diffractometer, using Cu Kα radiation (λ = 1. 54056Å). The patterns were scanned through steps of 0.02 (2θ) in the 2θ range 10-80°. Figure 2 shows the observed diffraction pattern of the sintered compound. Diffraction is a mathematical tool, which involves numerical computation, in order to obtain exact phase fraction and phase information. Indexing and phase quantification of powders was performed by means of the Search and Match and DICVOL [25] option available in X'pert High Score Plus.

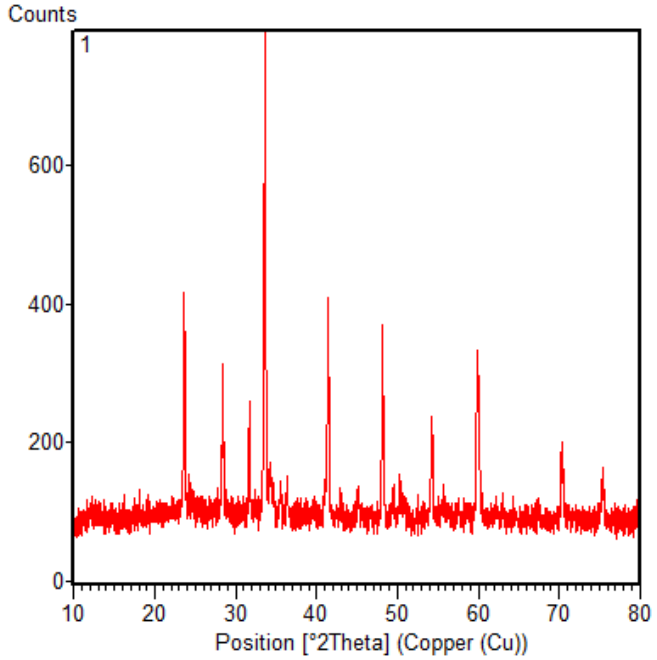


Figure 2 Observed profile of the diffraction data.

The Rietveld refinement of the pattern was carried out with the starting parameters of the phases. It was used to reduce the difference between experimental and calculated diffraction patterns. So, the parameters and peak profile were refined. The refinement was done using the following equation,

$$R = \frac{|Fobs - Fcalc|}{|Fobs|} \ldots . (1)$$

The refined data of the powder diffraction shows that only two binary states of $LaAlO_3$ and $La_2Zr_2O_7$ were present. So, neither $LaAl_{11}O_{18}$ (β-phase) nor any ternary state was present in the sintered compound. Figure 3 shows the Rietveld refined pattern of the sintered compound with indexed planes. Table 2 shows the Global parameters of the refined pattern. In Rietveld refinements, the Pseudo Voigt function was taken which uses the least square method to quantify the refined profile. The quantification of phases was indicated as R factor.

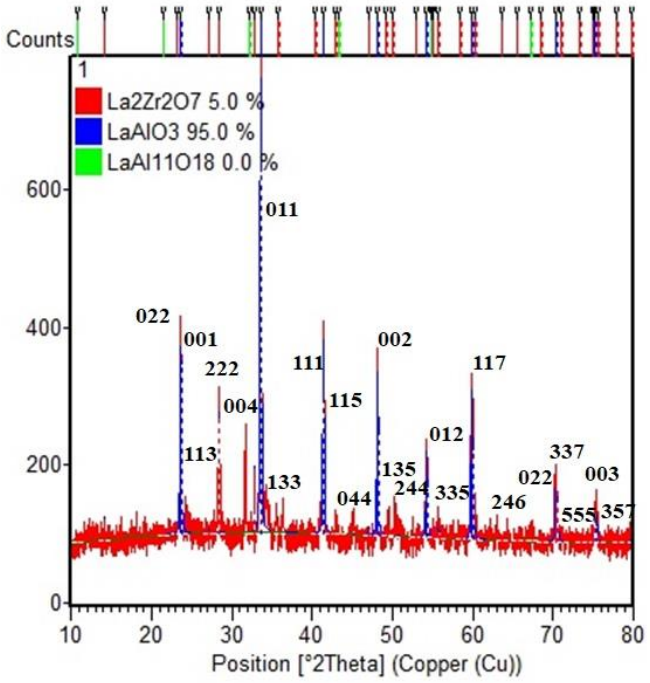


Figure 3 Fitted profile of $LaAlO_3$-$La_2Zr_2O_7$ powder.

Table 1. Diffraction data for $LaAlO_3$- $La_2Zr_2O_7$ powder.

S.No.	d-spacing	hkl	Phase	Lattice type	Space group
1.	3.8501	022	$La_2Zr_2O_7$	Face centered cubic	Fm-3m
2.	3.7644	001	$LaAlO_3$	Rhombohedral/Pseudo cubic	R3m
3.	3.2869	113	$La_2Zr_2O_7$	Face centered cubic	Fm-3m
4.	3.1478	222	$La_2Zr_2O_7$	Face centered cubic	Fm-3m
5.	2.7283	004	$La_2Zr_2O_7$	Face centered cubic	Fm-3m

6.	2.6674	011	$LaAlO_3$	Rhombohedral/Pseudo cubic	R3m
7.	2.5047	133	$La_2Zr_2O_7$	Face centered cubic	Fm-3m
8.	2.18	111	$LaAlO_3$	Rhombohedral/Pseudo cubic	R3m
9.	2.1028	115	$La_2Zr_2O_7$	Face centered cubic	Fm-3m
10.	1.9322	044	$La_2Zr_2O_7$	Face centered cubic	Fm-3m
11.	1.889	002	$LaAlO_3$	Rhombohedral/Pseudo cubic	R3m
12.	1.8479	135	$La_2Zr_2O_7$	Face centered cubic	Fm-3m
13.	1.8221	244	$La_2Zr_2O_7$	Face centered cubic	Fm-3m
14.	1.6903	012	$LaAlO_3$	Rhombohedral/Pseudo cubic	R3m
15.	1.6677	335	$La_2Zr_2O_7$	Face centered cubic	Fm-3m
16.	1.5435	112	$LaAlO_3$	Rhombohedral/Pseudo cubic	R3m
17.	1.5318	117	$La_2Zr_2O_7$	Face centered cubic	Fm-3m
18.	1.462	246	$La_2Zr_2O_7$	Face centered cubic	Fm-3m
19.	1.3373	022	$LaAlO_3$	Rhombohedral/Pseudo cubic	R3m
20.	1.337	337	$La_2Zr_2O_7$	Face centered cubic	Fm-3m
21.	1.2639	555	$La_2Zr_2O_7$	Face centered cubic	Fm-3m
22.	1.2611	003	$LaAlO_3$	Rhombohedral/Pseudo cubic	R3m
23.	1.2016	357	$La_2Zr_2O_7$	Face centered cubic	Fm-3m

The refined pattern shows the non-fused $LaAlO_3$of Rhombohedral/pseudocubic phase (R3m) and$La_2Zr_2O_7$ of cubic phase (Fm-3m). Table 1 shows the diffraction data for $LaAlO_3$- $La_2Zr_2O_7$ powder. We can confirm that there was no other phase present in the powder other than the binary phases. The peak positions (001), (011), (111), (002), (012), (022) and (003) show the pseudocubic type of crystal system matching with $LaAlO_3$, in which all the possible reflections occur. The other peaks were constituted by $La_2Zr_2O_7$the phase of the cubic crystal system. We can confirm the $La_2Zr_2O_7$ phase by its reflection condition of k+l, h+l, and h+k = even number (all hkl value must be either odd or even).

Table 2. Global parameters of Refined pattern.

Parameters	**Values/ Types**
Profile function	Pseudo Voigt
Background	Polynomial
R (expected)	9.7059
R (profile)	10.5017
R (Weighed profile)	13.9819
Goodness of fit	2.0752

The R weighed profile used to emphasize the intense peaks over the background profile and also 13.9819% values reliability shows that the refined pattern was perfectly fitted and refined parameters of each phase are shown in Table 3. Table 4 and 5 provides the absolute value of lattice parameters and atomic position.

Table 3: Refined parameter of each phase in $LaAlO_3$-$La_2Zr_2O_7$ powder.

S.No.	**Parameter**	**$LaAlO_3$**	**$La_2Zr_2O_7$**
1	Space group	R 3 m (Pm-3m)	F m – 3 m
2	Weight fraction %	95	5
3	a(Å)	3.7901	10.9660
4	b(Å)	3.7901	10.9660
5	c(Å)	3.7901	10.9660
6	α(◦)	90	90
7	β(◦)	90	90
8	γ(◦)	90	90
9	Volume Å^3)	54.4443	1318.6961

Table 4: Occupancy, Atomic Fraction Coordinates and B-iso of $LaAlO_3$.

Atom	**Wyck. off**	**X**	**Y**	**Z**	**B-iso**	**Occupancy**
La	1b	0.5	0.5	0.5	0.004	1
Al	1a	0	0	0	0.004	1
O	3c	0	0.5	0.5	0.014	1

Table 5: Occupancy, Atomic Fraction Coordinates and B-iso of $La_2Zr_2O_7$.

Atom	**Wyck. off**	**X**	**Y**	**Z**	**B-iso**	**Occupancy**

La	8a	0.125	0.125	0.125	0.2	1
Zr	8b	0.375	0.375	0.375	0.2	1
O1	16c	0	0	0	1	1
O2	32e	0.25	0.25	0.25	1	0.04
O3	96e	0	0	0.295	1	0.99

During the processing of oxides in solid-state reaction, they get fused with one another to form the binary phases. Therefore, they introduce strain in the matrix. The Williamson-Hall plot for strain and crystallite size was calculated using the Debye Scherrer formula,

$$D = \frac{K\lambda}{\beta \cos\theta} \quad \ldots.(2)$$

The lattice strain induced in powders due to crystal imperfection and distortion was calculated using formula [27],

$$\varepsilon = \frac{\beta\cos\theta}{\sin\theta} \quad \ldots.(3)$$

Table 6: Calculation of βcosθ and sinθ from 2θ values.

S.No.	2θ (°)	cosθ	sinθ	β (FWHM) (°)	βcosθ
1.	23.0823	0.9798	0.2001	0.01	0.000171
2.	27.1071	0.9722	0.2344	0.01	0.00017
3.	28.3294	0.9696	0.2447	0.01	0.00017
4.	32.7997	0.9593	0.2823	0.01	0.000168
5.	33.5702	0.9574	0.2888	0.1797	0.003011
6.	35.8219	0.9515	0.3075	0.01	0.000167
7.	41.3846	0.9355	0.3534	0.1631	0.00267
8.	42.9778	0.9305	0.3663	0.01	0.000163
9.	43.0894	0.9301	0.3672	0.01	0.000163
10.	46.9893	0.9171	0.3987	0.01	0.00016
11.	48.1302	0.9131	0.4078	0.1584	0.002531
12.	49.2732	0.909	0.4169	0.01	0.000159
13.	50.017	0.9063	0.4228	0.01	0.000159
14.	54.2226	0.8901	0.4557	0.1639	0.002553
15.	55.0172	0.8869	0.4619	0.01	0.000155
16.	60.3803	0.8644	0.5029	0.01	0.000151
17.	70.3045	0.8176	0.5758	0.2244	0.003211
18.	70.3583	0.8174	0.5761	0.01	0.000143
19.	75.1008	0.7928	0.6095	0.01	0.000139
20.	79.977	0.7762	0.6426	0.01	0.000136

Table 7: Crystallite size and Lattice strain value of $LaAlO_3$- $La_2Zr_2O_7$ powder.

Sample	Average Crystallite size (µm)	Lattice strain
$LaAlO_3$-$La_2Zr_2O_7$ powder	0.209 µm	$5x10^{-3}$

From table 6, 7, the $LaAlO_3$-$La_2Zr_2O_7$the powder has less strain induced in it since no fusion had been reported between the $LaAlO_3$ and $La_2Zr_2O_7$ phases. Therefore, no grain contraction has occurred in between the phases, resulting in less strain in the matrix. The crystallite size of the powder was a little bit high as from table 6 since the ball milling time was only 5 hours.

3.2. GFourier Mapping

The Fourier Mapping Program performed the electron charge density distribution for the diffraction pattern of the sample in a 2D plane. The refined result was used as input for the GFourier Program, available in FullProf. The program Fourier calculates the scattering density inside the unit cell of a crystal of whatever symmetry. It uses a Fast Fourier Transform (FFT) subroutine to accelerate the calculation of the following expression,

$$\rho(r) = \frac{1}{V}\sum_H F(H)\exp[-2\pi i\,(H.r)] \quad \ldots.(4)$$

Where V is the volume of the unit cell. H is a reciprocal lattice vector, r is a vector position inside the unit cell, and F(H) are complex Fourier coefficients used to perform different types of Fourier syntheses. Since $LaAlO_3$ was present as the major phase in diffraction pattern, it contributed to a higher extent in charge density while $La_2Zr_2O_7$to a lesser part. Therefore, the charge density mapping had shown most of distribution for $LaAlO_3$, while the charge density for $La_2Zr_2O_7$was not observed. Since there was no fusion between $LaAlO_3$ and $La_2Zr_2O_7$ in the powder, as seen in refined results, the mapping shown the charge distribution only for $LaAlO_3$. Figure 4 and 5 provides the charge density distribution of both phases across the x-y and x-z plane. The refined results did not show the mapping of $La_2Zr_2O_7$, since the weighed fraction of $LaAlO_3$ was very high in comparison with $La_2Zr_2O_7$.

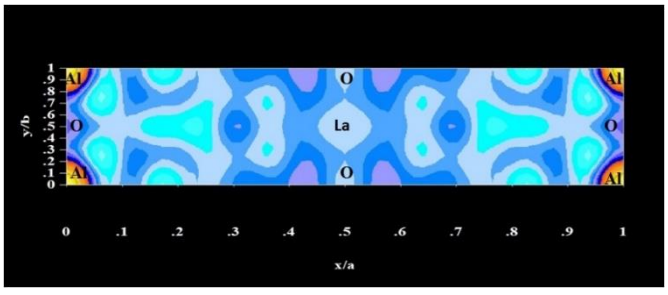


Figure 4 GFourier Mapping of charge density across x-y plane.

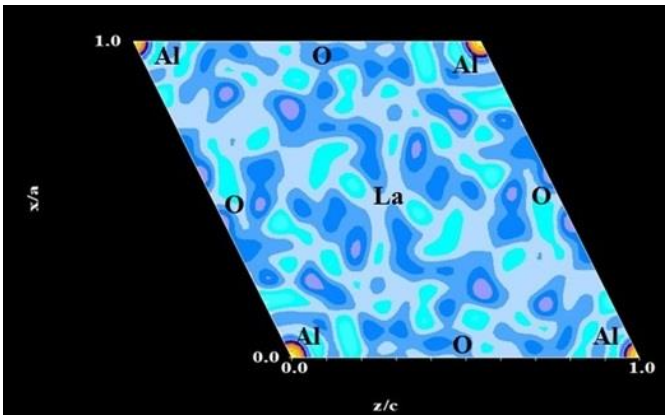


Figure 5 GFourier Mapping of charge density across x-z plane.

3.3. Charge density and Band structure calculation

In order to carry out the charge density and band structure calculations, the two phases of $LaAlO_3$ and $La_2Zr_2O_7$ were pattern decomposed by EXPO [26] and X'pert High Score Plus. The crystallographic information file for each phases quantified, was generated by X'pert High Score Plus. The values from table 6 and 7, were fed as input along with the crystallographic information file obtained from Rietveld refinement to Vesta software. In this, we have visualized the 3D crystal structure and studied the nature of its charge density, which shows stability of powder. After the calculation of charge density in VESTA for each phase, the crystallographic information file was taken as input for band structure calculation in BURAI. The results of each phase are described in detail.

3.3.1 $LaAlO_3$:

The physical unit cell of cubic $LaAlO_3$ phase was visualized in VESTA as shown in figure 6, which contains La^{3+}, Al^{3+} and O^{2-}at centre, corners and octahedral sites in a unit cell.

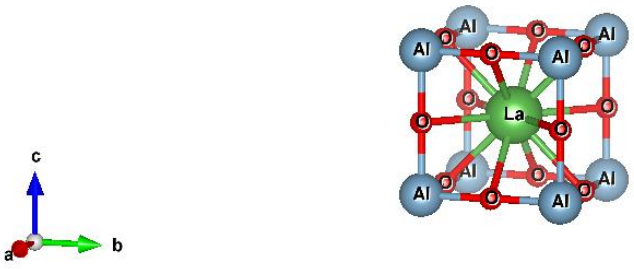


Figure 6 The Unit cell of $LaAlO_3$.

By visualization of the unit cell of $LaAlO_3$ in VESTA, we observed the various bond lengths and bond angle between various atoms, provided in table 8 and 9.

Table 8: Bond lengths between atoms of $LaAlO_3$ unitcell

S.No.	Atoms	Bond length
1	La - O	2.6805 Å
2	Al-O	1.8957 Å

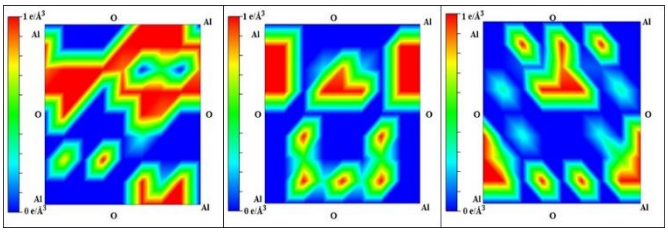
Table 9: Bond angles of $LaAlO_3$ unitcell

S.No.	Bonds	Bond angle
1	La-O-Al	90°
2	O-La-O	90°
3	O-Al-O	90°

Various electron density calculation was carried out for the $LaAlO_3$unit cell using VESTA software for the obtained structure factor. The electron density was first calculated for $LaAlO_3$ in every method by using the structure factor and for a resolution of 0.5Å. Then the mapping of electron densities were done using the 2D display option in VESTA. The distribution of charges between atoms present in the lattice was studied by Fourier synthesis of unit cells. The structure factors are obtained from the Rietveld refinement for each phase. Since the fourier transform of structure factor gives electron charge density. The electron density for a crystal at any point x, y,z represented by ρ(xyz) [28], can be calculated by,

$$\rho(xyz) = \frac{1}{V}\sum_{hkl} F(hkl)\exp[-2\pi i\,(hx + ky + lz)] \quad \ldots..(5)$$

Where, V is the volume for the unit cell and F hkl() is the structure factor for the particular set of indices h, k and l.


Figure 7: 2-D Mapping of Fourier synthesis of $LaAlO_3$ in the plane of [left] (001), [middle] (010) and [right] (100).

The 2-D electron density distribution in $LaAlO_3$ were drawn in the range of 0 to 1 e/Å^3 with interval 0.1 e/Å^3 for the (001), (010) and (100) planes as shown in

figure 7. We can observe that there is high amount of charge accumulation at the mid of the bond between the Al and O atoms. Therefore, we can confirm the presence of covalent bond between Al and O atoms, due to high electronegativity difference between them. There is also large amount of charge accumulation at the centre of each plane, representing the bonds between the La and O atoms. Here, the red region indicates the charge concentration whereas the blue region indicates vacancy. The model electron density was calculated by the Fourier transform of structure factors, F(h), that are calculated from structure parameters and atomic scattering factors of free atoms using the following expression [29],

$$\rho(x,y,z) = \sum_{h=\frac{-Nx}{2}}^{\frac{Nx}{2}} \sum_{k=\frac{-Ny}{2}}^{\frac{Ny}{2}} \sum_{l=\frac{-Nz}{2}}^{\frac{Nz}{2}} F(h) \exp[-2\pi i(hx + ky + lz)] \quad \ldots.(6)$$

Where Nx, Ny and Nz are number of grids along each crystallographic axis. These are automatically set such that it gives a resolution close to the specified value and that Nx satisfies symmetrical constraints. The spacial resolution of electron densities is specified in the unit of Å.

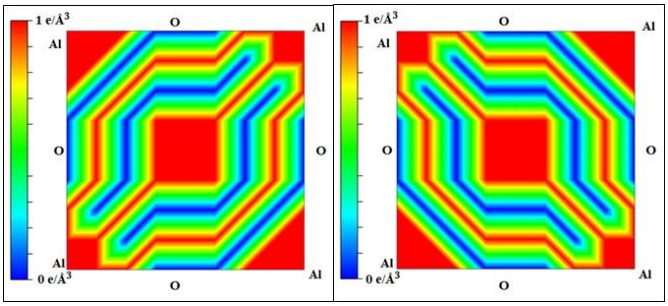


Figure 8: 2-D Mapping of Model electron densities of $LaAlO_3$ for [left] (001) and [right] (100) planes.

The model electron densities of $LaAlO_3$for the (001) and (100) plane were calculated with the spatial resolution of 0.5Å. The calculated 2-D model electron density distribution is given in figure .8. The electron density distribution was drawn for a range of 0-1 e/Å^3 with interval 0.1 e/Å^3. High accumulation of charges at center and the corner of the plane confirms that there was no vacancy, also the presence of covalent bonds between La-O and Al-O atoms. The Patterson electron density was calculated from the values of model electron density on providing the spatial resolution of 0.5Å. The Patterson electron density is given by the following equation [30],

$$\rho(x,y,z) = \sum_{h=\frac{-Nx}{2}}^{\frac{Nx}{2}} \sum_{k=\frac{-Ny}{2}}^{\frac{Ny}{2}} \sum_{l=\frac{-Nz}{2}}^{\frac{Nz}{2}} |F(h)|^2 \exp[-2\pi i(hx + ky + lz)] \quad \ldots.(7)$$

Figure 9 shows the 2-D mapping of Patterson electron density for the plane of (001) and (100) plane.

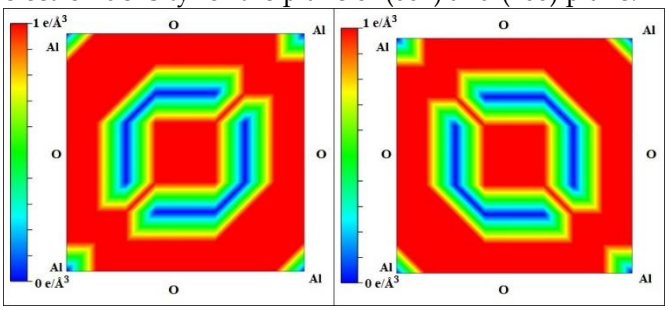


Figure 9: 2-D Mapping of Patterson electron density of $LaAlO_3$for [left] (001) and [right] (100) planes.

The 2-D mapping was drawn in the range of 0-1 e/Å^3 with interval 0.1 e/Å^3.In this mapping, we can observe that there is less vacancy across both the planes. By the high amount of charge concentration, we can confirm that the bonds are of covalent nature. Since these atoms share the electrons, we can observe this type of concentration regions. The vacant regions at the center of plane indicate there is no bonding between Al and La atoms. Then the conversion of electron densities was carried out in many methods.

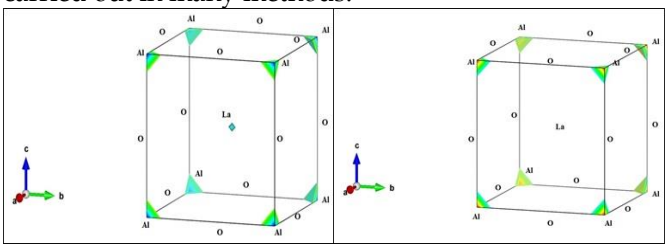


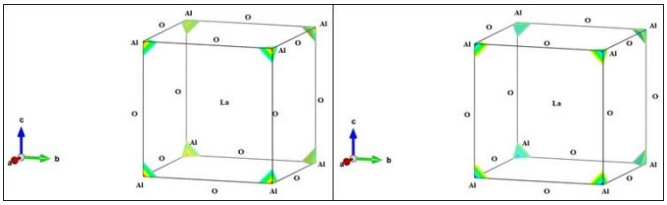
Figure 10: Laplacian of electron density (left) and Electronic Kinetic-energy density (right) of $LaAlO_3$.

The Laplacian of the electron density $\{\nabla^2\rho(r)\}$ was calculated from the electron density ρ(r) at the position vector r. It recovers the shell structure of an atom as several alternating shells of charge concentration and charge depletion. Thus, the analysis of the Laplacian provides information about the reactive sides of the phase. Figure 10 shows the Laplacian of electron density in 3-D.

The electronic kinetic-energy density g(r) was calculated by the following equation [31],

$$g(r) = \frac{h^2}{m}\left\{\frac{3}{10}(3\pi^2)^{\frac{2}{3}}[\rho(r)]^{\frac{5}{3}} + \frac{\lambda[\nabla\rho(r)]^2}{\rho(r)} + \frac{k\nabla^2\rho(r)}{2}\right\} \quad \ldots.(8)$$

where $h^2$is Dirac's constant, and m is the electron mass; the gradient $\hbar$-expansion of the green function around the classical Thomas-Fermi approximation [32] yields $\lambda = 1/72$ and $k = 1/6$. It provides information about electronic structure complementary to that provided by the local electron density. Figure 10 (b) describes the kinetic energy of localized electron pairs. By this, we can observe that the kinetic energies were localized at the corners i.e. Al atoms.



(a) **(b)**

Figure 11: Electronic potential-energy density (a) and Electronic energy density (b) of $LaAlO_3$.

The electronic potential-energy density v(r) was calculated by the following equation [31],

$$v(r) = \frac{h^2}{4m}\nabla^2\rho(r) - 2g(r) \quad \ldots.(9)$$

This mapping provides the indication of potential energies localized across the unit cell. Figure 11 (a) shows the distribution of potential energy at the Al atoms in $LaAlO_3$ unitcell. The electronic-energy density $h_e(r)$ is the sum of electronic potential v(r) and kinetic g(r) energy densities. Figure 11 (b) shows the distribution of total energy density across the $LaAlO_3$ unitcell. The natural logarithm of electron density is the probability density of electron from nucleus. As shown in figure 12, we can see the probability of electrons at the corners and centre of $LaAlO_3$unit cell.

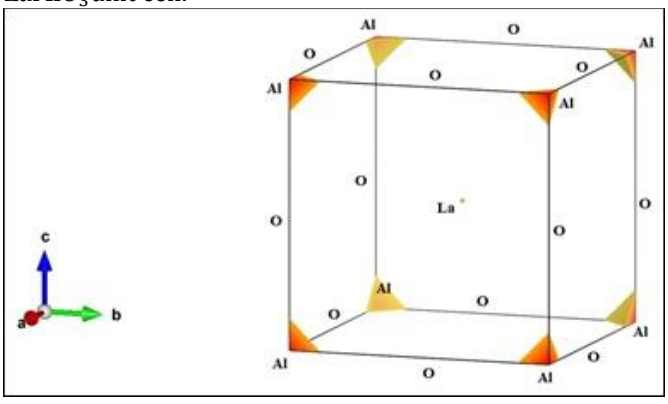


Figure 12: Natural logarithm of the electron density of $LaAlO_3$.

The peak positions in the volumetric data of $LaAlO_3$ phase were found with the Peak search option in VESTA. The results of peak search for electron densities in the perovskite-type $LaAlO_3$ are as follows,
Integrated value of volumetric data over the unit cell: 148.992962, -54.992964
Number of peaks in the volumetric data = 11
Number of voxels at Voronoi boundaries = 503/512

Table 10: Peak search results of $LaAlO_3$.

S.No.	x	y	z	Peak Value	Integrated value	Volume
1	0	0	0	197.4	64.29	2.874
2	0.5	0.5	0.5	33.6	11.93	6.812
3	0.375	0	0	22.15	-0.8638	4.275
4	0.625	0	0	22.15	-0.8638	4.275
5	0	0.375	0	22.15	-0.8638	4.275
6	0	0.625	0	22.15	-0.8638	4.275
7	0	0	0.375	22.15	-0.8638	4.275
8	0	0	0.625	22.15	-0.8638	4.275
9	0.5	0.5	0	14.66	7.654	6.386
10	0	0.5	0.5	14.66	7.654	6.386
11	0.5	0	0.5	14.66	7.654	6.386

Table 10 gives the peak values of electron density with their x, y and z coordinates. The Integrated value represents the number of electrons per site, which is calculated by summation of numbers of electrons over the Voronoi volume of the site.

3.3.2. $La_2Zr_2O_7$

The physical unit cell of cubic $La_2Zr_2O_7$phase was visualized in VESTA as shown in figure 13, which contains La^{3+}, Zr^{2+} and O^{2-}. The obtained unit cell differs from the pyrochlore structure in the arrangement of atoms [38]. Due to solid state reaction synthesis of raw materials in 2:2:1 ratio, the oxygen atoms have been fused together at some points in the unit cell. The $La_2Zr_2O_7$obtained in the powder is offused and transition state. The Lanthanum and zirconium are also observed alternatively in position.

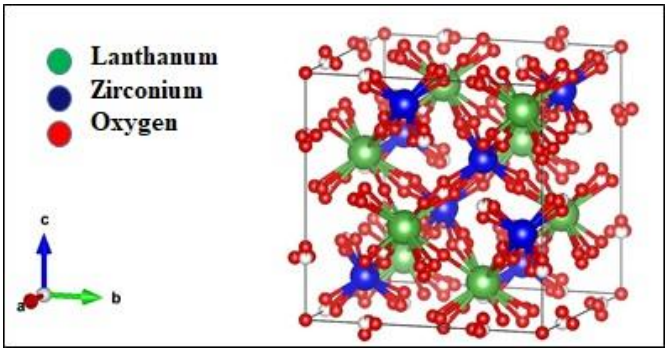


Figure 13. The unit cell of $La_2Zr_2O_7$.

By the visualization of the unit cell of $La_2Zr_2O_7$ in VESTA, we observed the various bond lengths and bond angle between various atoms, provided in table 11 and 12.

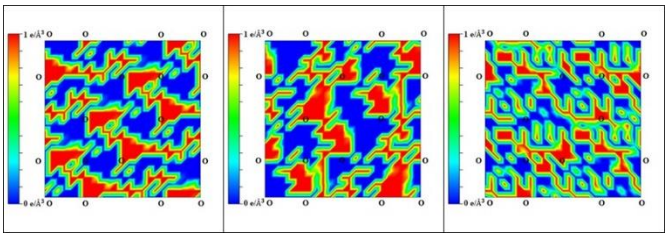
Table 11: Bond lengths between atoms of $La_2Zr_2O_7$ unitcell

S.No.	Atoms	Bond length (Å)
1	La-O1	2.3402
2	La-O2	2.3402
3	La-O3	2.651
4	Zr-O2	2.3402
5	Zr-O3	2.097

Table 12: Bond angles of $La_2Zr_2O_7$ unitcell.

S.No.	Atoms	Bond angle (°)
1	O1-La-O2	70.5288
2	O1-La-O3	66.4
3	O2-La-O3	8.62
4	O2-Zr-O3	10.92

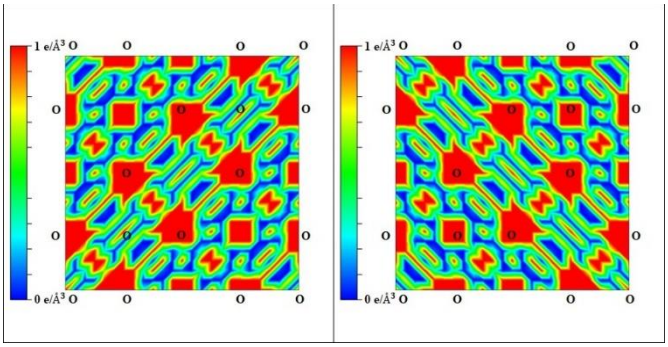
Various electron density calculations were carried out for the $La_2Zr_2O_7$unit cell using VESTA software for the obtained structure factor. The electron density was first calculated for $La_2Zr_2O_7$ in every method, as done for $LaAlO_3$by using the structure factor and for a resolution of 0.5Å. Then the mapping of electron densities were done using the 2D display option in VESTA. First, the distribution of electron charge was studied in Fourier synthesis method for $La_2Zr_2O_7$ from the obtained structure factors. Figure 14[a], [b] and [c] shows the electron density distribution in $La_2Zr_2O_7$ across (001), (010) and (100).



(a) (b) (c)

Figure 14: 2-D Mapping of Fourier synthesis of $La_2Zr_2O_7$in the plane of [a] (001), [b] (010) and [c] (100).

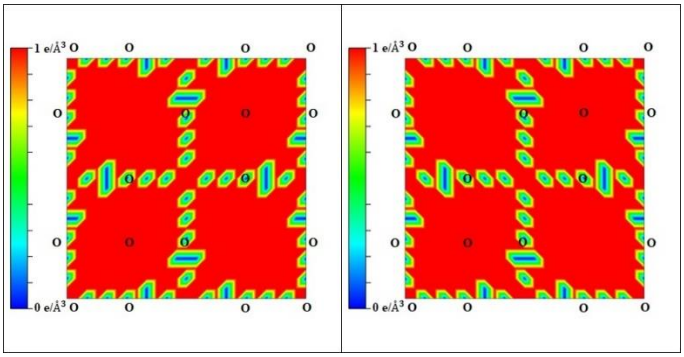
The 2-D electron density distribution in $La_2Zr_2O_7$were drawn in the range of 0 to 1 e/Å^3 with interval 0.1 e/Å^3. We can observe that there is high amount of vacancies across the plane, indicated by blue region. It is mainly due to the smaller atomic radii of oxygen (0.74Å) in comparison to La (1.88Å) and Zr (1.6Å). Here, the red region indicates the charge concentration i.e. where the Zr and La atoms are positioned in between O atoms. All the planes considered only of O atoms, while the Zr and La atoms are present at the interstitial positions of $La_2Zr_2O_7$ unit cell. Thus, we can confirm that the bonds between the atoms are of covalent nature, due to charge accumulation between the bonds.



(a) (b)

Figure 15: 2-D Mapping of Model electron densities of $La_2Zr_2O_7$for [left] (001) and [right] (100) planes

The model electron densities of $La_2Zr_2O_7$for the (001) and (100) plane were calculated with the spatial resolution of 0.5Å. The calculated 2-D model electron density distribution is given in figure 15 [a] and [b]. The electron density distribution was drawn for a range of 0-1 e/Å^3 with interval 0.1 e/Å^3. High amount of vacancy can be observed and also the presence of covalent bonds between atoms due to charge density between bonds.

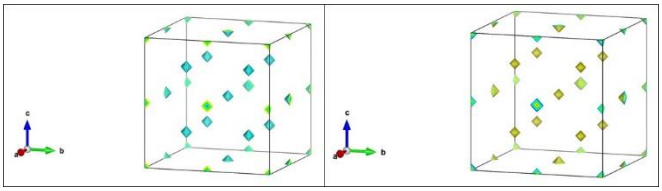


[a] [b]

Figure 16: 2-D Mapping of Patterson electron density of $La_2Zr_2O_7$for [a] (001) and [b] (100) planes

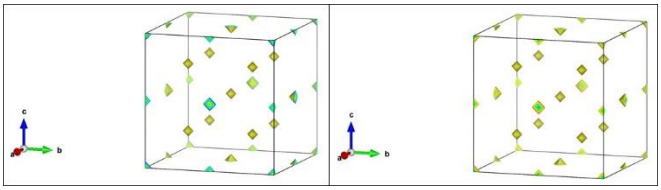
Electron charge density calculations were next carried out with the Patterson method. The figure 16 shows the 2-D mapping of Patterson electron density for the plane of (001) and (100) plane. The 2-D mapping was drawn in the range of 0-1 e/Å^3 with interval 0.1 e/Å^3.In this mapping, we can observe that there is less vacancy across both the planes. By the high amount of charge concentration, we can confirm that the bonds are of covalent nature. Since these atoms share the electrons, we can observe this type of concentration regions. The vacant regions at the plane indicate the non-bonding between Zr-O1 and La-Zr.

Then the conversion of electron densities of the $La_2Zr_2O_7$phase was carried out in many methods to find the Laplacian [17(a)], Kinetic-energy density [17(b)], potential-energy density [18(a)], Electronic energy density [18(b)] and Natural logarithm of electron density [figure 19]. The indexing of atoms was not done due to the complexity in unitcell of $La_2Zr_2O_7$.



(a) (b)

Figure 17: Laplacian of electron density(a) and Electronic Kinetic-energy density (b) of $La_2Zr_2O_7$



(a) (b)

Figure 18: Electronic potential-energy density (a) and Electronic energy density (b) of $La_2Zr_2O_7$.

Laplacian of electron density shows that the all La^{3+}, $Zr^{2+}$and O^{2-} are reactive sites in $La_2Zr_2O_7$. The kinetic and potential energy diagrams show that all three ionic sites have some amount of energy stored in them, leading to the total electronic-energy density. Natural logarithm of electron density shows the probability of electrons in unitcell, where it is mainly seen at the O^{2-} sites.

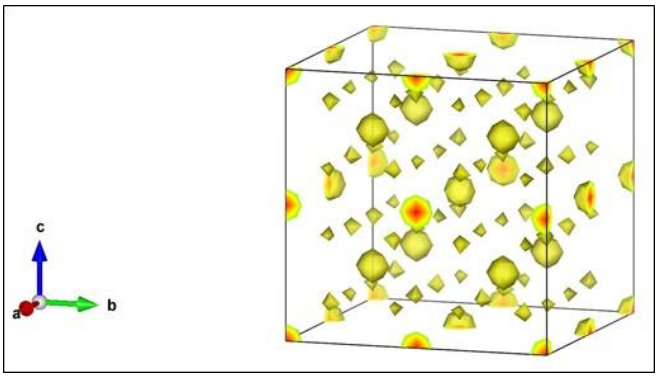


Figure 19: Natural logarithm of the electron density of $La_2Zr_2O_7$.

The peak positions in the volumetric data of $La_2Zr_2O_7$phase were found with the Peak search option in VESTA. The results of peak search for electron densities in the pyrochlore structure are as follows,

Integrated value of volumetric data over the unit cell: 2877145.952867, -72994.739029

Number of peaks in the volumetric data = 488

Number of voxels at Voronoi boundaries = 8858/13824

Table 13: Peak search results of $La_2Zr_2O_7$

S.No.	x	y	z	Peak value	Integrated	Volume
1	0	0	0	103000	267000	130
2	0.5	0.5	0	103000	267000	130
3	0.5	0	0.5	103000	267000	130
4	0	0.5	0.5	103000	267000	130

5	0.25	0.25	0.25	93500	263000	114
6	0.75	0.25	0.25	93500	263000	114
7	0.25	0.75	0.25	93500	303000	129
8	0.75	0.75	0.25	93500	303000	129
9	0.25	0.25	0.75	93500	303000	129
10	0.75	0.25	0.75	93500	303000	129

Table 13 gives the peak value of electron density with their x, y and z coordinates. The Integrated value represents the number of electrons per site, which is calculated by summation of numbers of electrons over the Voronoi volume of the site.

3.4. TEM Investigations

3.4.1 TEM analysis of sintered compacts

Morphology of Al_2O_3-ZrO_2-La_2O_3 powder particles with high spatial resolution in the sintered conditions was analyzed using TEM imaging mode. The phase contrast (dark and light regions) due to the density difference between the lanthanum aluminate ($LaAlO_3$) and lanthanum zirconate ($La_2Zr_2O_7$) phases (figure 20). Lanthanum aluminate has a higher density than lanthanum zirconate. Darkfield imaging was used since the density difference is vast and the scattered electron will be lost in the bright field mode while observing the distribution of powder particles. TEM images reveal that the particles were homogenous and ensure that the powders are suitable for spray deposition. The average particle size of the 5 hr milled and sintered powder was 0.7325 µm while for 10 hr sample was 0.4687 µm and for 15 hr sample was 0.4150µm (table 14). Edges appear to be faceted inconsistent directions. The orientation differences between the particles were observed, and the degree of misorientation appears to be very low. In order to identify the orientation of each faces the angles between the particles were measured in 'Image J software.' Two hypotheses have been found from the present investigation of the powder particle,

1. A typical reconstructive type of image is generally seen which indicates a flat interface.
2. Clustering of particles along the edges and corners indicate the particle size were predominantly small that leads to the attraction between the particles and consequent agglomeration.

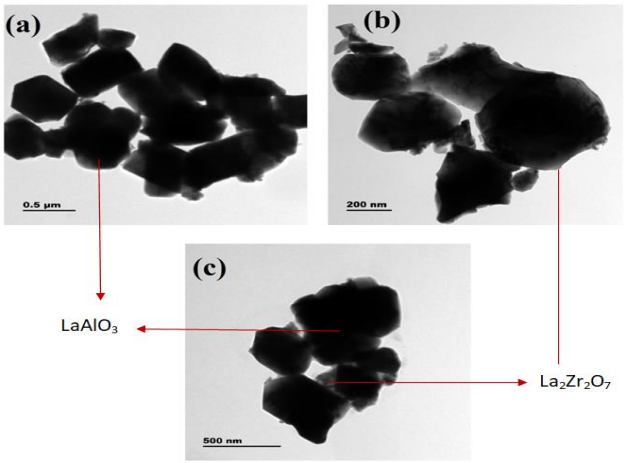


Figure 20: TEM Micrograph sintered particles (a) 5 hr milled (b) 10 hr milled (c) 15 hr milled sample.

Table 14: Particle size obtained from the TEM image.

Sample	Particle size (µm)			
5 hr	0.647	0.740	0.333	0.8325
10 hr	0.483	0.358	0.458	0.574
15 hr	0.418	0.453	0.465	0.325

Lattice imaging of each phase was observed using HRTEM and identified using the fringe pattern (figure 21). A large number of lattice fringes are seen caused by originating from the interference of phase difference between the electron beams. These fringes have the same spacing throughout the lattice planes but different orientations. Few interfaces are seen between the continuity of the lattice planes, and those continuities show a certain degree of coherency throughout the pattern. Distinct fringe patterns like Moiré fringes were also present in the image obtained. The angle between two different orientations measured in the figure 14(a) contains 90° which corresponds to the planes (10-1) and (222) whilefigure 14 (b) showed 71° which corresponds to the planes (10-1) and (331) and figure 14 (c) showed an angle of 90° between the planes (-101) and (111). The layer boundaries are distinct from each phase (i.e.,) ($LaAlO_3$) and ($La_2Zr_2O_7$). The presence of preferred orientation was seen, which is also colored to differentiate the change in preferred orientation in different directions as seen in figure 14.

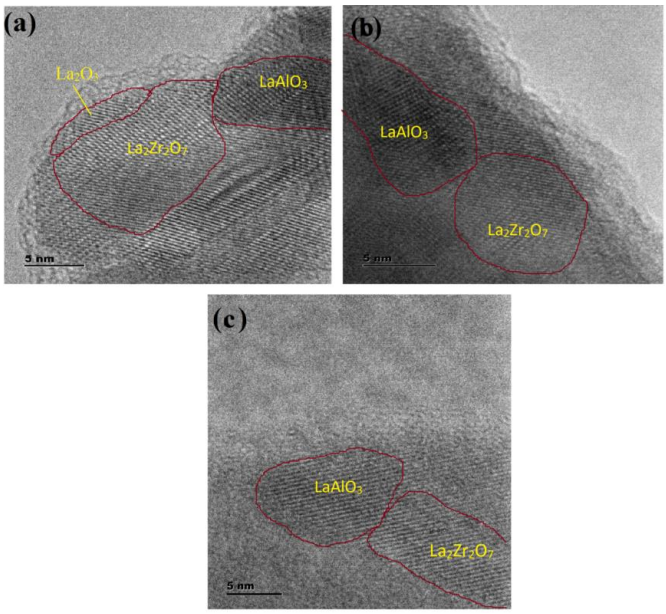


Figure 21: HRTEM image from the sintered powder (a) 5 hr milled (b) 10 hr milled (c) 15 hr milled sample.

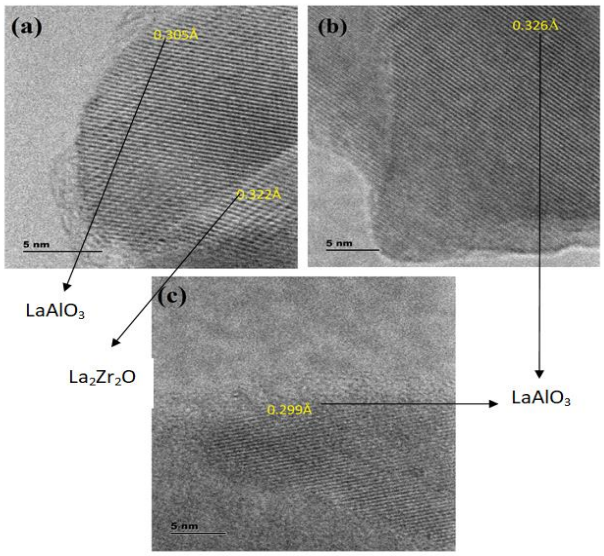


Figure 22 High-resolution lattice image from Al_2O_3-ZrO_2-La_2O_3.

Generally, crystalline materials will have preferred orientations. Each preferred orientation is considered as a grain. Presence of significant orientations could be seen clearly. The presence of many grains with its preferred orientation confirms that the powders are crystalline (poly-crystalline) in nature. Figure 22 shows the HRTEM fringe pattern from which the interplanar spacing (d-spacing value) can be easily determined. The measured lattice spacing shown in figure 15 (a) were 0.305Å, and 0.322 Å correspond to (10-1) plane. Both (10-1) planes and (222) planes correspond to Lanthanum aluminate ($LaAlO_3$) phase and Lanthanum zirconate ($La_2Zr_2O_7$) phase respectively. These indicate that the procured powder contains the expected phase and the existences of both the phases are distinct by their orientation of the atom shown in figure 22 (a). Figure 22 (b) 10 hr sample contains the lattice spacing of 0.346 Å which corresponds to (111) plane. (111) representing he Lanthanum Aluminate ($LaAlO_3$) phase. 15 hr milled and sintered sample shown in figure 22 (c) has the lattice spacing of 0.299 Å which corresponds to (10-1) plane representing the $LaAlO_3$ phase. The ordered pattern (in fig 22) indicates periodicity is confirming the crystalline nature of the material.

3.4.2 Selected area electron diffraction pattern (SAD)

Figure 23 shows the Selected Area Diffraction pattern for sintered Al_2O_3-ZrO_2-La_2O_3 milled at a different time. Inter-planar spacings of 0.3013 Å and 0.2941 Å shown in figure 23 (a) were obtained using the software C spot diffraction, and the corresponding planes were found to be (10-1) and (0-11) obtained from the manual indexing. The plane is seen in figure 23 (a) corresponds to Lanthanum Aluminate ($LaAlO_3$) phase having a rhombohedral crystal structure R-3c. The reflections from the {110} family of the plane can be observed in the 5 hr milled and sintered powder sample. The inter-planar spacing was calculated using Braggs law ($2d\sin\theta=n\lambda$), and the angle between the two planes was found to be 120°. The resultant plane is (1-10) which has an inter-planar spacing of 0.2953 Å.

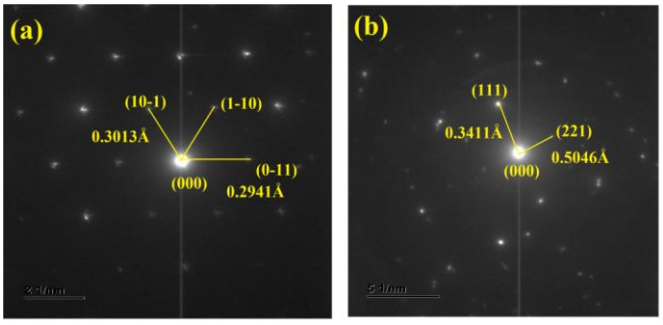


Figure 23 SAED pattern for Al_2O_3-ZrO_2-La_2O_3 powder after sintering (a) 5 hr milled sample (b) 10 hr milled sample.

The inter-planar spacing for 10 hr sample has 0.3411 Å and 0.5046 Å those values (figure 23 (b)). The resultant (hkl) values have been calculated as (111) and

(221) planes respectively. The angle between these two planes is 90˚, and the calculated (hkl) values match the values of Lanthanum Aluminate ($LaAlO_3$) phase. The planes and their corresponding phases were verified for space group R-3c and their corresponding atomic position obtained from the XRD results. From figure 25 (a) the preferred orientation matches with the zone axis [-1-1-1] and for figure 25 (b) zone axis was found to be [-110]. Figure 24 shows that the spotty ring pattern which indicates the sample is nanocrystalline with a preferred orientation. The inter-planar spacing for 15 hr sample has 0.3203 Å and 0.3661 Å. These zone axes were calculated manually and compared with the zone axis simulated using Winwulff software©. The zone axes calculated for 5hr, 10hr, and 15 hr samples agreed with the simulated stereographic projection shown in figure 25 (a), (b) and (c) respectively.

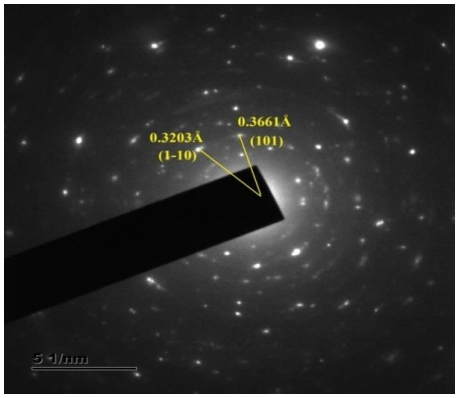


Figure 24 SAED pattern for 15hr milled and sintered sample.

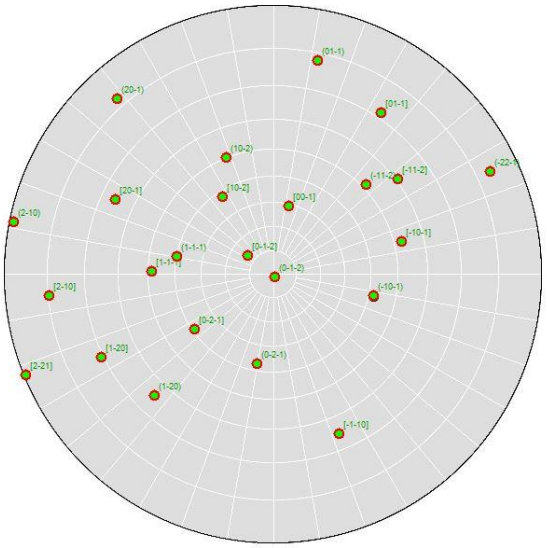


Figure 25(a).[-1-1-1] zone axis stimulated using Winwulff© software.

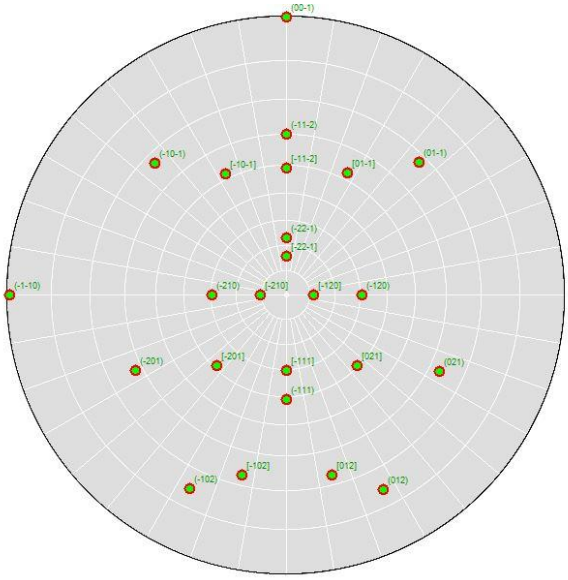


Figure 25(b) [-110] zone axis stimulated using Winwulff© software.

3.4.3 EDS analysis of Al_2O_3-ZrO_2-La_2O_3 samples

Energy Dispersive Spectroscopy (EDS) was carried out for elemental analysis characterization of Al_2O_3-ZrO_2-La_2O_3 compacts. Cu kα having a wavelength of 1.54 Å was used. EDS results obtained for different milling time (figure 26 (a) (b) and (c)) and corresponding element present in the powders are shown in table 15(a) (b) (c).The relative amount of elements present in the analyzed powder contains only Al, Zr, La and oxygen. The element Cu which comes from the grid used for analyzing the powder sample in HRTEM. Results confirmed the purity of the sample after sintering.

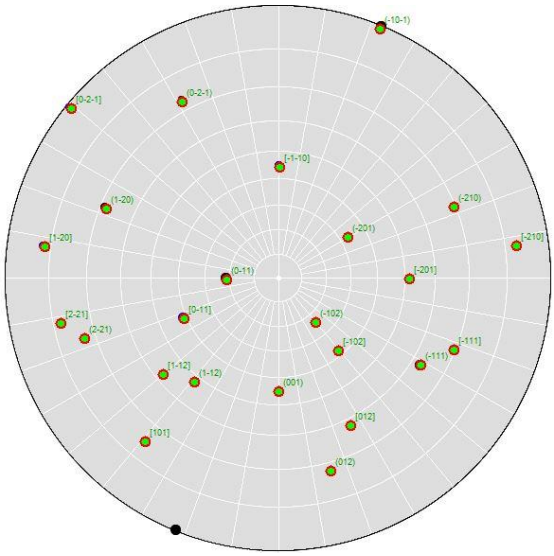


Figure 25(c) [-1-11] zone axis stimulated using Winwulff© software.

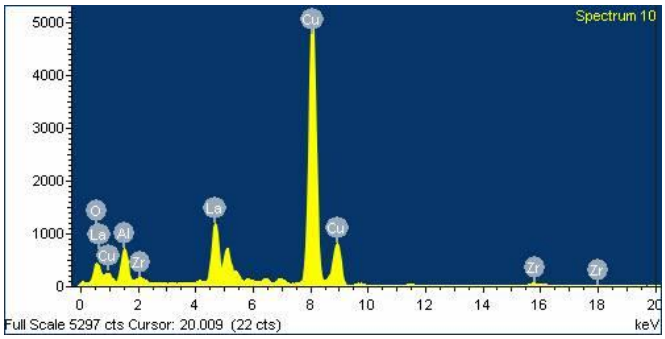


Figure 26 (a) EDS of sintered Al_2O_3-ZrO_2-La_2O_3 powder with milling time of 5 hr

Table 15 (a) Relative amount of elements present in 5 hr milled sample

Element	Al	Zr	La	O	Cu
Atomic%	5.26	0.33	11.9	4.88	77.59
Weight%	2.07	0.44	24.26	1.14	72.09

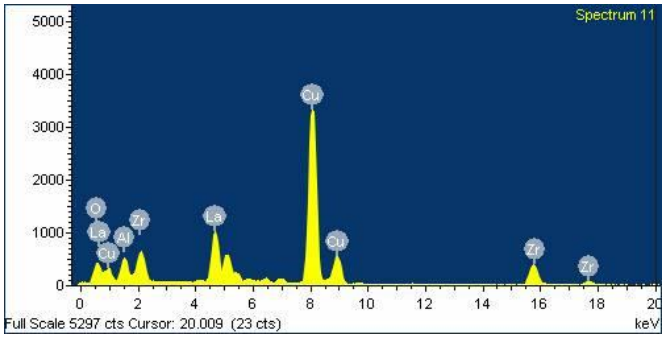


Figure 26 (b) EDS of sintered Al_2O_3-ZrO_2-La_2O_3powder with milling time of 10 hr

Table 15 (b) Relative amount of elements present in 10 hr milled sample

Element	Al	Zr	La	O	Cu
Atomic%	4.40	3.57	14.08	6.29	71.67
Weight%	1.68	4.62	27.72	1.43	64.55

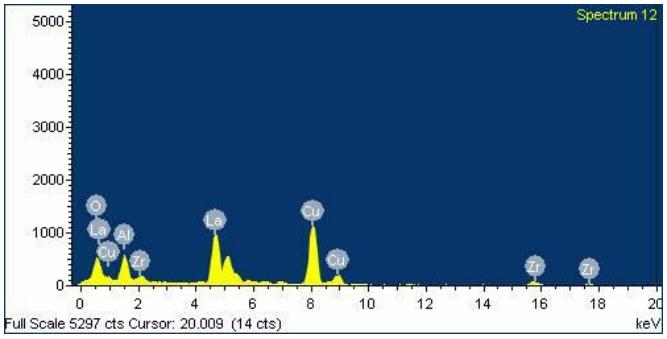


Figure 26 (c) EDS of sintered Al_2O_3-ZrO_2-La_2O_3 powder with milling time of 15 hr.

Table 15 (c) Relative amount of element present in 15 hr milled sample.

Element	Al	Zr	La	O	Cu
Atomic %	9.89	1.47	26.74	15.64	46.27
Weight %	3.65	1.84	50.85	3.42	40.24

5. CONCLUSION

$LaAlO_3$ and $La_2Zr_2O_7$ were prepared by wet ball milling and sintered upto 1300°C. Rietveld refinements showed that they crystallized in rhombohedral/pseudo cubic ($LaAlO_3$) and face centered cubic ($La_2Zr_2O_7$) structures. In this, $LaAlO_3$ exhibited a pseudocubic structure possessing the lattice parameters equal to that of rhombohedral structure. Quantification of phases were done, which shows that $LaAlO_3$ of 95% and $La_2Zr_2O_7$ of 5%. No fused structure was formed in the synthesized powder, resulting in separate binary phases and less lattice strain (0.0005) induced in between them. Electronic density calculations based on structure factors of phases revealed that covalent bonds were found between atoms at$LaAlO_3$ and $La_2Zr_2O_7$unitcell. Band structure and DOS calculation based on self-consistent field (SCF) included in the Quantum Espresso show $LaAlO_3$ as an indirect wide bandgap semiconductor material.

References

1. Zhang, Q., & Saito, F. (2000). Mechanochemical synthesis of lanthanum aluminate by grinding lanthanum oxide with transition alumina. Journal of the American Ceramic Society, 83(2), 439–441. https://doi.org/10.1111/j.1151-2916.2000.tb01215.x
2. Li, Z., Zhang, S., & Lee, W. E. (2007). Molten salt synthesis of $LaAlO_3$ powder at low temperatures.

Journal of the European Ceramic Society, 27(10), 3201–3205. https://doi.org/10.1016/j.jeurceramsoc.2007.01.008
3. Kakihana, M., & Okubo, T. (1998). Low-temperature powder synthesis of $LaAlO_3$ through an in situ polymerization route utilizing citric acid and ethylene glycol. Journal of Alloys and Compounds, 266(1–2), 129–133. https://doi.org/10.1016/S0925-8388(97)00445-3
4. Tian, Z.-Q., Yu, H.-T., & Wang, Z.-L. (2007). Combustion synthesis and characterization of nanocrystalline $LaAlO_3$ powders. Materials Chemistry and Physics, 106(1), 126–129. https://doi.org/10.1016/j.matchemphys.2007.05.027
5. Jones, D. M. (2007). Sensitive detection of mirror symmetry by CBED applied to $LaAlO_3$ and $GdAlO_3$. Acta Crystallographica Section B: Structural Science, 63(1), 69–74. https://doi.org/10.1107/S0108768106045381
6. Silveira, I. S., Ferreira, N. S., & Souza, D. N. (2021). Structural, morphological and vibrational properties of $LaAlO_3$ nanocrystals produced by four different methods. Ceramics International, 47(19), 27748–27758. https://doi.org/10.1016/j.ceramint.2021.06.201
7. Brylewski, T., & Bućko, M. M. (2013). Low-temperature synthesis of lanthanum monoaluminate powders using the co-precipitation–calcination technique. Ceramics International, 39(5), 5667–5674. https://doi.org/10.1016/j.ceramint.2012.12.083
8. Dias, L. P. S., Oliveira, J. S., Marques, G. N., Araújo, T. R., Melo, D. M. A., Cabral, A. A., Vasconcelos, J. S., Rangel, J. H. G., Bernardi, M. I. B., & Figueredo, G. P. (2024). Structural, morphological, and optical investigations of Mn-doped $LaAlO_3$ perovskite obtained by microwave-assisted combustion and rapid calcination at low temperature. Materials Chemistry and Physics, 325, Article 129767. https://doi.org/10.1016/j.matchemphys.2024.129767
9. Filonova, E., & Medvedev, D. (2022). Recent progress in the design, characterisation and application of $LaAlO_3$- and $LaGaO_3$-based solid oxide fuel cell electrolytes. Nanomaterials, 12(12), Article 1991. https://doi.org/10.3390/nano12121991
10. Vassen, R., Cao, X., Tietz, F., Basu, D., & Stöver, D. (2000). Zirconates as new materials for thermal barrier coatings. Journal of the American Ceramic Society, 83(8), 2023–2028. https://doi.org/10.1111/j.1151-2916.2000.tb01506.x
11. Cao, X. Q., Vassen, R., Jungen, W., Schwartz, S., Tietz, F., & Stöver, D. (2001). Thermal stability of lanthanum zirconate plasma-sprayed coating. Journal of the American Ceramic Society, 84(9), 2086–2090. https://doi.org/10.1111/j.1151-2916.2001.tb00962.x
12. Minervini, L., Grimes, R. W., & Sickafus, K. E. (2000). Disorder in pyrochlore oxides. Journal of the American Ceramic Society, 83(8), 1873–1878. https://doi.org/10.1111/j.1151-2916.2000.tb01484.x
13. Jarligo, M. O. D., Kang, Y.-S., & Kawasaki, A. (2005). Physicochemical properties of single-phase $La_2Zr_2O_7$ powder. Materials Transactions, 46(2), 189–192. https://doi.org/10.2320/matertrans.46.189
14. Huang, Z., Li, F., Jiao, C., Liu, J., Huang, J., Lu, L., Zhang, H., & Zhang, S. (2016). Molten salt synthesis of $La_2Zr_2O_7$ ultrafine powders. Ceramics International, 42(5), 6221–6227. https://doi.org/10.1016/j.ceramint.2016.01.004
15. Chen, H., Gao, Y., Liu, Y., & Luo, H. (2009). Coprecipitation synthesis and thermal conductivity of $La_2Zr_2O_7$. Journal of Alloys and Compounds, 480(2), 843–848. https://doi.org/10.1016/j.jallcom.2009.02.081
16. Zhang, A., Lu, M., Zhou, G., Wang, S., & Zhou, Y. (2006). Combustion synthesis and photoluminescence of Eu^{3+}, Dy^{3+}-doped $La_2Zr_2O_7$ nanocrystals. Journal of Physics and Chemistry of Solids, 67(11), 2430–2434. https://doi.org/10.1016/j.jpcs.2006.05.004
17. Xu, J., Zhong, X., Ouyang, R., Gong, Y., Liu, Y., Xu, X., Fang, X., & Wang, X. (2023). Preparation of $La_2Zr_2O_7$ composite oxides with fluorite/pyrochlore phases by excluding element influences for catalyzing oxidative coupling of methane. Physical Chemistry Chemical Physics, 25(40), 27045–27052. https://doi.org/10.1039/D3CP03508E
18. Sui, T., Feng, Q., Luo, N., He, J., Huang, H., Yuan, C., Cen, Z., & Chen, X. (2024). New pyrochlore $La_2Zr_2O_7$ ceramics with ultra-high breakdown electric field strength and energy storage efficiency. Journal of Materials Chemistry C, 12(23), 8426–8434. https://doi.org/10.1039/D4TC01912A
19. Lei, Z., Zhang, X., Zhang, S., Zhu, G., Zhao, Y., Liu, L., & Xu, H. (2025). Preparation of $La_2Zr_2O_7$ nanopowders via a novel tartaric coprecipitation method. Ceramics International, 51(19, Part A),

28455–28459. https://doi.org/10.1016/j.ceramint.2025.04.016
20. Liu, B., Wang, J. Y., Zhou, Y. C., Liao, T., & Li, F. Z. (2007). Theoretical elastic stiffness, structure stability and thermal conductivity of $La_2Zr_2O_7$ pyrochlore. Acta Materialia, 55(9), 2949–2957. https://doi.org/10.1016/j.actamat.2006.12.035
21. Rietveld, H. M. (1969). A profile refinement method for nuclear and magnetic structures. Journal of Applied Crystallography, 2(2), 65–71. https://doi.org/10.1107/S0021889869006558
22. Rodríguez-Carvajal, J. (1993). Recent advances in magnetic structure determination by neutron powder diffraction. Physica B: Condensed Matter, 192(1–2), 55–69. https://doi.org/10.1016/0921-4526(93)90108-I
23. Momma, K., & Izumi, F. (2011). VESTA 3 for three-dimensional visualization of crystal, volumetric and morphology data. Journal of Applied Crystallography, 44(6), 1272–1276. https://doi.org/10.1107/S0021889811038970
24. Altomare, A., Cuocci, C., Giacovazzo, C., Moliterni, A. G. G., & Rizzi, R. (2006). Powder diffraction: The new automatic least-squares Fourier recycling procedure in EXPO2005. Journal of Applied Crystallography, 39(4), 558–562. https://doi.org/10.1107/S0021889806017912
25. Jeevanantham, N., Rangasamy, B., Prasanna, S., & Velauthapillai, D. (2026). Structural refinement, charge density mapping and microstructural analysis of $Sb_2(S,Se)_3$ thin films. Zeitschrift für Kristallographie – Crystalline Materials. Advance online publication. https://doi.org/10.1515/zkri-2025-0065.